Tribol Lett (2012) 47:467–480
DOI 10.1007/s11249-012-0006-9

ORIGINAL PAPER

In Situ Film-Forming and Friction-Reduction Mechanisms for Carbon-Nanotube Dispersions in Lubrication

V. Chauveau · D. Mazuyer · F. Dassenoy · J. Cayer-Barrioz

Received: 21 May 2012 / Accepted: 22 June 2012 / Published online: 7 July 2012

Abstract Current requirements in automotive lubrication impose extremely complex formulation. For environmental reasons, it is important to reduce or eliminate the presence of sulphur and phosphorus contained in tribological additives. For that purpose, multi-walled carbon nanotubes have been dispersed in oil in various concentrations. The lubrication mechanisms of such dispersions in mixed and EHL regimes have been investigated by means of the IRIS tribometer that allows us simultaneous contact visualization, film thickness and friction measurement under controlled contact kinematics. The lubricant film-forming capability has been determined as a function of the entrainment velocity and the nanotube content: the presence of carbon nanotubes within the contact results in a local increase in the film thickness and it can be shown that the contact acts as a filter of carbon-nanotube aggregates. Introduction of sliding results in a diminution of the number of aggregates passing through the contact. Moreover, a reduction in friction and a drift in the wear onset have been observed under controlled contact kinematics: this behaviour originates from the transient propagation of carbon-nanotube aggregates through the contact and a friction law is proposed taking into account the contact heterogeneity.

Keywords Additives · EHL · Friction mechanisms

V. Chauveau · D. Mazuyer · F. Dassenoy · J. Cayer-Barrioz (✉)
LTDS, CNRS UMR5513, Ecole Centrale de Lyon, 36 Avenue Guy de Collongue, 69134 Ecully Cedex, France
e-mail: juliette.cayer-barrioz@ec-lyon.fr

V. Chauveau
Total France, Centre de Recherches de Solaize, BP 22, Chemin du Canal, 69360 Solaize, France

1 Introduction

Due to environmental requirements in automotive lubrication formulation, innovative additives have been widely investigated in recent years. In parallel, there has been considerable interest in the development of nanotechnologies, leading to the consideration of nanoparticles as lubricant additives. Many lubricating oils already contain solid particles [1]: the latter are present either by accident as in the case of soot [2–7] or debris contaminants or deliberately added, to improve the lubricant performance.

These colloidal systems, as defined by Ostwald [8], contain particles whose characteristic size ranges from 1 nm to 10 μm. The organization of these particles in the suspension depends on the nature of the interaction forces [9] such as Van der Waals interactions, electrostatic interactions (especially in aqueous media), Brownian interactions and steric interactions. These forces together with the hydrodynamic interactions due to shear rate govern the rheological behaviour and thus the flow properties of these colloidal fluids.

In a lubricated interface, these fluids experience velocity and pressure fields as well as confinement due to the low ratio between the film thickness and the contact characteristic length. The particle mobility is then modified: interactions and intermittent contacts between particles are more or less likely to happen and be more or less severe, leading to a possible phenomenon of dynamic aggregation [4–6]. This directly impacts the ability of the colloidal fluid to penetrate within the contact and to contribute to load bearing. On the other hand, friction behaviour is related to the ability of the colloidal fluid to create a hydrodynamic and/or boundary (physi- or chemisorbed) friction film. Friction results from the collective and heterogeneous intra- and interparticle shearing. The friction response is

thus controlled by the organization of the particles and by their microstructure.

Many studies have focused in the past years on the use of solid particles dispersed into greases, oil [1–7, 10–12] or aqueous lubricants [13–15]. They reveal that one of the major criteria to consider is the size of the solid particles compared to the film thickness. For particles larger than the film thickness, particle behaviour is mainly controlled by the contact kinematics conditions [10–13]. At low entrainment velocity, particles are easily trapped into the contact where they deform plastically and form an adherent boundary film. This film disappears with a velocity increase. At higher velocity, the particles are rejected from the contact and the number of particles reaching the conjunction remains low. This induces a diminution of the film thickness. Introduction of sliding acts very similarly. At high slide-to-roll ratio (SRR) [12], lubricant film rupture may occur and wear appears on the surfaces. An interpretation of these mechanisms based on the analysis of the flow and reflow zones in the contact inlet and their evolution with entrainment and sliding velocities was proposed by Chinas-Castillo and Spikes [1]. These studies highlight the importance of particle-trapping mechanisms within the contact. Other parameters also need to be taken into account, such as the nature of the particles and their concentration, their ability to deform, their affinity with the surfaces, and the nature of the surfactant that controls the adhesion between the particles and the surfaces. In the case of nanoparticles or thick lubricant films, the particles are entrained by the fluid flow and penetrate easily in the contact, independently of the contact kinematics. In a first step, the nanoparticles come into the contact to form a third body, thanks to the surfactants adsorbed onto their surfaces [13, 14]. The presence of high surface asperities can create nanoparticle reservoirs that continuously feed the contact [16]. Under shear, the particles plastically deform to form a compact viscous layer [13, 14, 17]. Finally, under severe temperature and/or pressure conditions, a tribofilm results from the reaction of the nanoparticles and the surfaces. This film may be strongly adherent and withstands shearing [18, 19]. The ability of inorganic nanoparticles (alumina, zinc borate, titanium oxide, magnesium borate) as efficient additives has been widely studied in the past years [17, 18, 20–22]. Inorganic fullerenes (IF) like nanoparticles made of metal dichalcogenides such as IF-MoS_2, IF-WS_2, and IF-NbS_2 are also well known for their lubricating properties when dispersed in water or oil [16, 19, 23–25]. The lubrication mechanism of these IF-nanoparticles was widely investigated [23, 24, 26]. The lubricating properties of the IF-nanoparticles were attributed to a gradual exfoliation of the external sheets of the particles during the friction process leading to their transfer onto the reciprocating surfaces and the formation of a 5-nm thin tribofilm. This tribofilm results from the reaction of the exfoliated layers and the surfaces [27].

If carbon is well known for its lubricating properties both in the form of graphite and as in diamond-like carbon, the discovery of Kroto et al. [28] enlarges the spectrum of use of carbon components in tribology. New forms of carbon such as fullerenes, onions and nanotubes generate widespread interest, especially because of their morphology and their chemical inertness [29]. However, contradictory results were obtained for fullerenes C60 as a function of temperature [30] and humidity [31]. Experimental results obtained for fullerenes dispersed in polyalphaolefin (PAO) base oil [24] showed that their lubricating properties may be related to the fullerenes ability to destructure and form a tribofilm onto the surface. Carbon onions were also tested as additives [23] and it seems that they exfoliate within the contact under severe tribological conditions. It was shown in [32] that crystallinity and number of defects in the nanoparticle structure played a key role in controlling friction.

At the nanometer scale, the friction of carbon nanotubes has been investigated using the AFM technique [33, 34]. Falvo et al. [33] observed the stick–slip rolling motion of an individual carbon nanotube on graphite. They showed that adhesion hysteresis was the dominant energy loss responsible for the stick–slip dynamics. They also measured a uniform friction between the carbon nanotube and the graphite substrate along the tube. Ohmae et al. [34] studied the friction of a gold tip over nanotube forest. This combination gave high friction and low adhesion. Computational simulations [35, 36] of a contact between aligned nanotubes and a diamond surface have been performed. At low contact pressure, Ni and Sinnott [36] observed that nanotubes slide in the contact, while at high contact pressure they were flattened and could both slide and roll according to their orientation and bonding to the sliding surface. Nevertheless, the occurrence of rolling in the contact is still under discussion [35, 37]. Regarding carbon-nanotube dispersions, a few authors [24, 38, 39] focused on their tribological performance in the boundary lubrication regime as a function of their structure (single- or multi-wall), their concentration and the presence of surfactants. The key role of the surfactant on dispersion stability was also confirmed by Chen et al. [39] and Saint-Aubin et al. [40].

The study described in this article addresses the lubrication mechanisms of carbon-nanotube dispersions in terms of film-forming ability and friction behaviour in the elastohydrodynamic lubrication regime. We use a tribometer that allows for the simultaneous measurement of the film thickness and its distribution and the contact forces under controlled contact kinematics. By doing so, we precisely describe the propagation kinetics of carbon

nanotubes in the contact and determine the effect of concentration as well as that of entrainment and shear on the film-forming mechanisms. Finally, we propose a simple model of the sheared interface that can account for our experimental friction data and demonstrate the role of carbon-nanotube aggregates on low frictional properties.

2 Experimental

2.1 The Carbon-Nanotube Dispersions

As solid nanoparticles, carbon nanotubes exist in various structures and lengths. In this article, we study multi-walled carbon nanotubes dispersed into base oil. The carbon nanotubes have an external diameter of about 11 ± 2 nm and an internal diameter of 5 ± 2 nm, according to TEM observations (see Fig. 1). Each layer of graphene can be distinguished and reaches 0.3 nm. The carbon nanotubes were analysed by means of the EELS technique using a LEO 912 TEM at 120 keV. Figure 2 presents the level K of carbon of a multi-walled nanotube. It clearly shows a separation between the conduction states π^* and σ^*, respectively, located at 285.3 and 292 eV. The existence of the peak π^* is a signature of carbon *sp*2 and the location of the peaks π^* and σ^*, close to that of graphite at, respectively, 284 and 292 eV, confirms the graphitic structure of the nanotubes. The length of the nanotubes is difficult to assess. However, it varies with the grinding time: the longer the grinding process, the shorter the nanotubes. In our case, a grinding time of 16 h was chosen resulting in a carbon nanotube length of 500 nm.

The carbon nanotubes were dispersed into a PAO base oil of viscosity equal to 53 mPa s at 23 °C. The carbon nanotubes and the PAO base oil were kindly supplied by Nanocyl and Total, respectively. The complex behaviour of the dispersions is related to the presence of nanoparticles in a simple liquid phase and it varies with the particle concentration. The concentration of carbon nanotubes ranged from 0.01 to 0.5 % (w/w). In order to avoid sedimentation phenomena, the dispersions were ultrasonicated for 30 min before an experiment. For such concentrations, the dispersions rheology was examined using an Anton Paar MCR51 rheometer in coaxial cylinder configuration. The dispersions are Newtonian up to shear rates of 1,000 s^{-1} and their viscosity slightly increases with the concentration from 53 to 66 mPa s, as shown in Fig. 3.

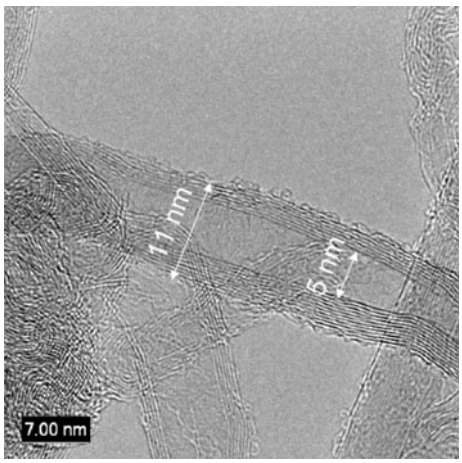

Fig. 1 TEM observation of a nanotube. The multi-walled structure is clearly shown and the external (respectively, internal) diameter is 11 ± 2 nm (respectively, 5 ± 2 nm)

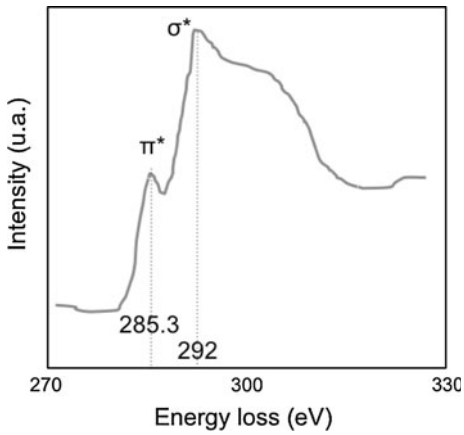

Fig. 2 EELS spectrum realized on a multi-walled nanotube. The level K of carbon is presented and it shows separated π^* and σ^* peaks, respectively, at 285.3 and 292 eV. This confirms the graphitic structure of the nanotube

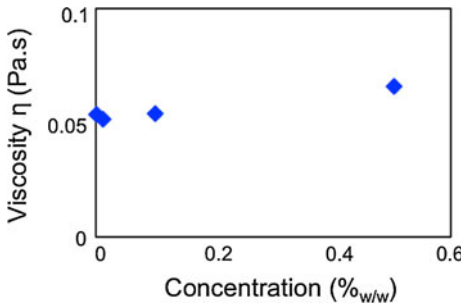

Fig. 3 Evolution of the viscosity (at ambient pressure) η of the dispersion as a function of the nanotube concentration

2.2 The IRIS Visualization and Friction Measurement Set-Up

The film-forming ability and the frictional properties of the dispersions are investigated using a home-made tribometer, named IRIS, coupling in situ contact visualization to friction measurements. This apparatus produces a lubricated contact between a sphere and a transparent semi-reflective

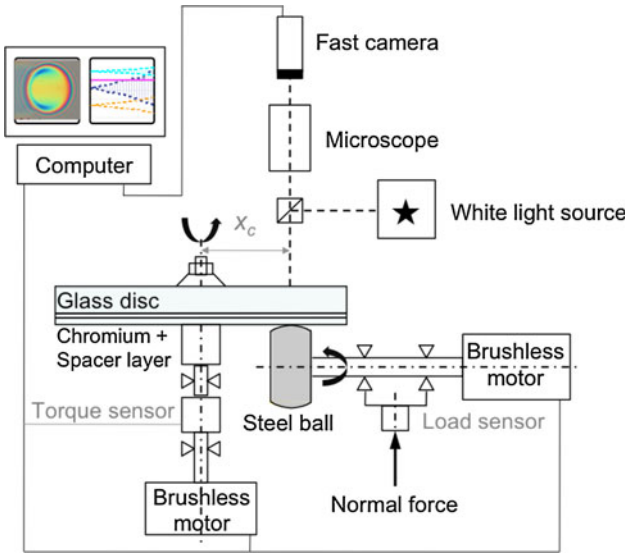

Fig. 4 Principle of the IRIS visualization and friction measurement set-up. The steel ball and silica disc velocities can be accurately and independently controlled by two brushless motors in the range 25 μm/s to 3 m/s. The normal load can be varied between 0 and 20 N. This set-up enables the simultaneous measurement of friction and visualization of the contact thanks to a high-speed recording camera

glass disc. It allows one to determine simultaneously the spatial and temporal variations of the interfacial lubricant film thickness using high-speed imaging technology while measuring the normal and tangential–frictional–contact forces with perfectly controlled contact kinematics. Figure 4 illustrates the principle of the IRIS set-up that has been described previously in detail in [41, 42].

The optical cavity formed between the two solids (lubricated sphere/disc contact) permits an accurate measurement of the film thickness distribution, from colour pictures acquired with a high-speed numerical CMOS recording camera using an interferometry technique. The spatial resolution is about 1 μm. Taking into account the refractive index of the fluids, a thickness resolution of few nanometres is obtained. In addition to film thickness distribution in the contact, this set-up permits the visualization of the convergent zone as well as the divergent zone and allows one to follow the propagation of aggregates with time towards, through and around the contact. The rotational motion of the two solids is monitored precisely and independently. Thus, numerous contact conditions (pure rolling conditions as well as sliding experiments) can be generated by varying the linear velocity of the surfaces between 25 μm/s and 3 m/s. The normal load w is continuously measured using a static force sensor in the range 0–20 N. A torque sensor, between the disc and its brushless motor, measures the friction coefficient during each experiment.

In the results presented here, a lubricated contact is established between a 19-mm-diameter steel ball and a 60-mm-diameter silica disc coated with a 10-nm-thick semi-reflective chromium layer and a 200-nm-thick spacer layer. The load is maintained constant at 15 N, leading to a 248 μm Hertzian contact diameter and a resulting mean contact pressure of 305 MPa, assuming the elastic properties of the two solids in Table 1. AFM measurements give the roughness, R_{ad}, of the silica disc at 5 nm while that of the steel ball, R_{ab}, is about 10 nm. The test surfaces are cleaned with heptane and then isopropyl alcohol in an ultrasonic bath for 10 min before use.

Table 1 Geometrical and elastic properties of the steel ball and the silica disc

	R (mm)	Roughness Ra (nm)	E (GPa)	v
Steel	9.5	10	210	0.30
Silica	∞	5	70	0.17

2.3 Experimental Procedure

The film thickness is measured using an interferometry technique. Each wavelength in the white light spectrum is partially reflected either by the semi-reflective chromium layer or by the steel ball. The reflected beams interfere to give a colour, which, after a calibration procedure, can be directly related to the film thickness. The calibration procedure is performed by imaging a static contact between the steel ball and the disc under a load w of 15 N. The correlation between contact interferograms in static conditions and the theoretical deformation of the steel ball allows the correlation between the RGB or HIS colour parameters and the gap between the two solids. From the data of Table 1, the geometry of the deformed ball can be determined [43] as a function of the ball radius R, the Hertzian contact radius a_H and the distance from the contact centre. Thus, knowing the lubricant refractive index, the relationship between the colour and the thickness of the film can be determined.

The film-forming capability is first tested under pure rolling conditions with entrainment velocity $U_e = (U_b + U_d)/2$ varying from 10^{-3} to 1 m/s, where U_b and U_d are the velocities of the ball and the disc, respectively ($U_b = U_d$ for pure rolling conditions). The evolution of the central film thickness is measured with entrainment velocity. Each dot corresponds to an averaged value over three images. Moreover, the in situ visualization associated with the high-speed imaging system allows one to follow the motion of nanotubes aggregates whose size is larger than the spatial resolution. Experiments at constant entrainment velocities of 20 and 60 mm/s are carried out to assess the velocity profile of an aggregate through the contact.

The frictional behaviour of the lubricants is determined by means of traction experiments. The sliding velocity U_s is defined as $U_s = U_b - U_d$. During such a friction experiment, the ball and the disc velocities as well as the normal force and frictional torque, are continuously measured. The velocities of the ball and the disc are controlled independently. Therefore, it is possible to control the SRR, defined as $\text{SRR} = U_s/(2U_e) = (U_b - U_d)/(U_b + U_d)$. These experiments are carried out at a constant entrainment velocity U_e of 20 mm/s to maintain a constant lubricant supply in the contact for SRR ranging from 0 to 100 %, which corresponds to U_s varying from 0 to 40 mm/s. In order to take into account the Couette contribution of the friction only [41, 44], one must subtract the Poiseuille contribution arising from the pressure difference between the inlet zone and the inner part of the contact zone. To do this, two steps are required. First, during a given time $t = 200$ s, the ball velocity is lower than that of the disc and the measured torque is referred to as C^-. In a second step and for a same duration time of 200 s, the ball velocity is fixed at a higher value than that of the disc. The measured torque is noted C^+.

The measured sliding friction μ_{sliding}, corresponding to the same SRR, is then calculated from the average of both torques C^- and C^+

$$\mu_{\text{sliding}} = \left(\frac{C^- + C^+}{2}\right)\frac{1}{w\,x_c}, \quad (1)$$

where w is the normal load and x_c is the distance between the centre of the contact zone and the disc axis (see Fig. 4). Each value of μ_{sliding} reported corresponds to an averaged value of three experiments.

All the experiments presented in this study are performed at room temperature (23 °C).

3 Results

3.1 Film Formation at Low Concentration

In the case of dispersions, at high entrainment velocity the contact interferogram illustrated in Fig. 5a for a 0.01 % (w/w) concentration is homogeneous and very similar to that obtained with the base oil. However, at lower velocity, thickness heterogeneities appear on the contact interferograms (see Fig. 5b). These are associated with the presence of carbon-nanotube aggregates. The latter are also visible in the convergent zone. Under pure rolling conditions, Fig. 6 plots the evolution of the central film thickness as a function of the entrainment velocity for the base oil and carbon-nanotube dispersions with concentrations of 0.01 and 0.1 % (w/w). The central film thickness of the base oil increases with entrainment velocity with a power law of

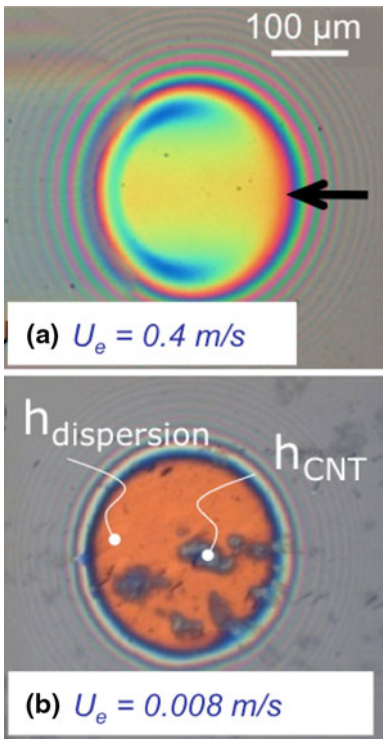

Fig. 5 Contact interferograms for the 0.01 % (w/w) dispersion **a** at high entrainment velocity $U_e = 0.4$ m/s where the classical EHL film distribution is observed. The *black arrow* indicates the flow direction from the right to the left. **b** at low entrainment velocity $U_e = 0.008$ m/s where two thicknesses can be defined as the central film thickness $h_{\text{dispersion}}$ and the maximum film thickness h_{CNT} attributed to the carbon-nanotube aggregates

2/3, obeying thus the prediction of Hamrock–Dowson [45] for a bulk viscosity of 53 mPa s in a continuous line.

A strong assumption is made regarding the refractive index of the dispersion since we consider the refractive index of the dispersion as equal to that of the carbon-nanotube aggregate. Additionally, to evaluate the impact of carbon nanotubes on the film thickness, two characteristic thicknesses are defined:

- the mean film thickness at the contact centre formed by the dispersion represented by full symbols in Fig. 6,
- the maximum film thickness corresponding to the thickness due to the aggregate of carbon nanotubes within the contact zone, represented by empty symbols in Fig. 6. This thickness is only measured at low velocity.

The curves corresponding to the mean central film thickness obtained for concentrations of both 0.01 and 0.1 % (w/w) are superimposed to that of the base oil for entrainment velocities down to 0.02 m/s, in good agreement with the values of bulk viscosity and Hamrock–Dowson calculation for Newtonian homogeneous fluids. This suggests that this film thickness formation is governed

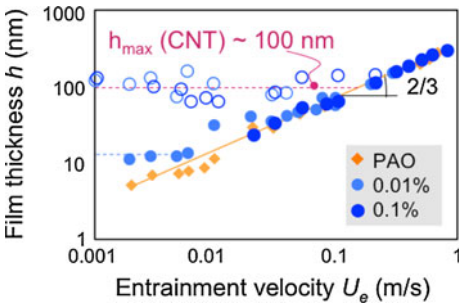

Fig. 6 Pure rolling experiment: central film thickness evolution with entrainment velocity U_e for the PAO base oil (*filled triangle*) and the low concentrated dispersions (0.01 % (w/w) in *pale blue filled circle* and 0.1 % (w/w) in *darker blue filled circle*). The central film thickness is presented in *full symbols*, while the thickness attributed to the passage of carbon nanotube is plotted with *empty symbols*. Each symbol corresponds to an average value over three images. The Hamrock–Dowson prediction is plotted in a *continuous line* and fits the experimental data for the base oil. At high velocity, the viscosity of the dispersions controls the central film thickness. At low velocity, the central film thickness stabilizes at around 10 nm. Moreover, a critical maximum film thickness of about 100 nm can be defined independently of the dispersion concentration (Color figure online)

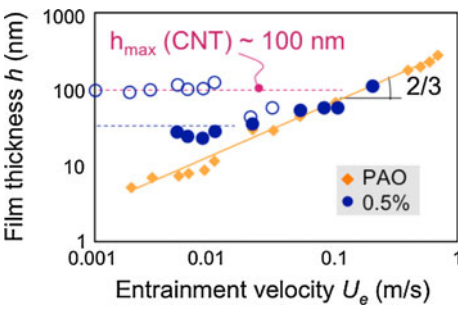

Fig. 7 Effect of high concentration (0.5 % (w/w)) on the evolution of the film thickness vs entrainment velocity U_e. The PAO base oil curve is also plotted for comparison. The film thickness for the 0.5 % (w/w) dispersion is lower than predicted. At low entrainment velocity, the central film thickness remains constant at approximately 20 nm. A critical maximal film thickness of about 100 nm can also be defined

by the viscosity, as predicted by EHL theory. At lower velocities, the central film thickness is slightly higher than the predicted one and it stabilizes at around 10 nm for the 0.01 % (w/w) dispersion.

However, a striking result is observed for maximum film thickness at entrainment velocities lower than 0.1 m/s in that this film thickness remains constant at about 100 nm, independently of the dispersion concentration. This can be either the signature of carbon-nanotube aggregates that adhere to the surfaces and penetrate into the contact or the signature of a critical size of aggregates, which is filtered by the contact. In either case, it results in a local increase in film thickness.

3.2 Film Formation at High Concentration

Figure 7 presents the dependence of the film thickness with entrainment velocity for the dispersion concentrated at 0.5 % (w/w). The curve corresponding to the PAO base oil is also indicated for comparison. It can be seen that the central film thickness still increases with the velocity. However, for velocities higher than 0.02 m/s, the measured central film thickness is lower than predicted with Hamrock–Dowson; for instance, the film thickness expected with a viscosity of 66 mPa s reaches 154 nm at $U_e = 0.2$ m/s while the measured one is only 94 nm. Contact interferograms obtained at $U_e = 0.4$ m/s show a homogeneous contact, as illustrated in Fig. 8a. However, the presence of an air/lubricant meniscus is depicted in the inlet zone leading to possible starvation mechanisms at high velocity. Starvation occurrence may be related to the

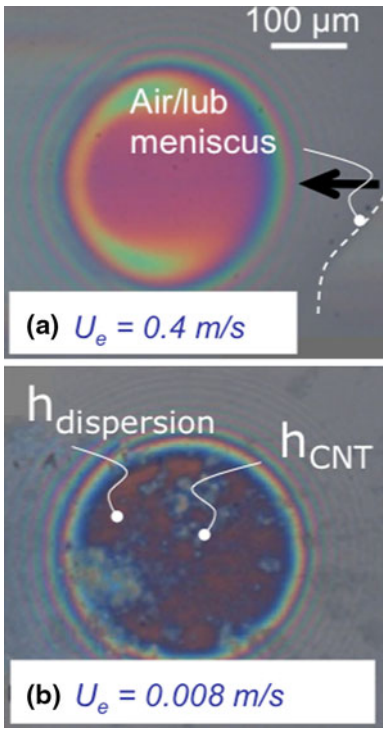

Fig. 8 Contact interferograms for the 0.5 % (w/w) dispersion **a** at high entrainment velocity $U_e = 0.4$ m/s where the classical EHL film distribution is observed. The *black arrow* indicates the flow direction from the right to the left while the *dashed lines* emphasize the position of the air/lubricant meniscus in the inlet zone and **b** at low entrainment velocity $U_e = 0.008$ m/s where two thicknesses can be defined as the central film thickness $h_{dispersion}$ and the maximum film thickness h_{CNT} attributed to the carbon-nanotube aggregates. Numerous aggregates can be seen in the inlet zone

heterogeneity of the highly concentrated dispersion and also to its more complex rheology, enhanced by entangled carbon nanotubes [29]. This hypothesis seems confirmed in Fig. 8b, where the contact interferogram at $U_e = 0.008$ m/s clearly shows a strong heterogeneity in thickness and the existence of a large aggregate. Another explanation for the

lower than expected film thickness might be the formation of a nanotube blockage/aggregation in the convergent zone: only base oil and small aggregates would be able to go through that blockage, leading to a decrease in viscosity for the lubricating fluid.

Figure 7 shows that the maximum film thickness remains constant with velocity at roughly 100 nm. Also note that at low velocity, the central film thickness stabilizes at approximately 40 nm for this concentration of nanotubes.

Results from Figs. 6 and 7 seem to indicate that the size of the aggregates that propagate within the contact is independent of the concentration. Moreover, the central film thickness at low velocities (slower than 0.02 m/s) diverges from Hamrock–Dowson prediction since it remains constant while the velocity varies and the stabilized value seems to increase with the carbon-nanotube content.

3.3 Transient Propagation of Carbon-Nanotube Aggregates Through the Contact

Carbon nanotubes are chemically inert. Also, there is no evolution of the film thickness with time at a constant entrainment velocity. This confirms that adsorption of carbon nanotubes on the surfaces is unlikely. The in situ visualization clearly demonstrates that carbon nanotubes move into the high pressure contact zone, as illustrated in Fig. 9a–e in pure rolling at $U_e = 0.02$ m/s for a dispersion of 0.1 % (w/w). The arrow indicates the aggregate traverses the convergent zone on its way to the contact zone in Fig. 9a. From Fig. 9b–d, one can see that the aggregate penetrates the contact and propagates in a direction parallel to the flow before it leaves. Figure 9e indicates the position of the aggregate in the divergent zone where no full lubricant film separates the surfaces. However, in this zone, its exact position relatively to the disc or the ball surfaces cannot be located. A local transient increase in film thickness, due to the passage of the aggregate, propagates through the contact. The time between two interferograms is 5 ms. This leads to an estimate of the velocity of the aggregate, as shown in Fig. 10. The entrainment velocity of the solids at 0.02 m/s is also plotted in a dashed line for comparison. The mean velocity of the aggregate seems to be lower than the entrainment velocity of the solids. Moreover, it varies with the position in the contact and seems slower in the first contact half width than in the second one. This result is independent of the velocity as a similar evolution is obtained at $U_e = 0.06$ m/s. However, due to the lack of precision in these local velocity measurements, it can be concluded that the velocity of the aggregate is of the same order of magnitude as that of the solid surfaces.

Only few studies have focused on local propagation velocity in an EHL conjunction. Reddyhoff et al. [46] observed that for pure rolling conditions, in the EHL regime, the lubricant travels through the contact with a velocity lower than the entrainment in the first half of the contact and higher in the second half, using fluorescence microscopy. Meunier [6] also refers to a slowdown of a lubricant dimple formed in reciprocating conditions at the point of zero velocity. In the latter case, this observation might be related to the transient contact kinematics. Nevertheless, the origins of these observations are still unclear. One can mention either the viscoelastic properties of the

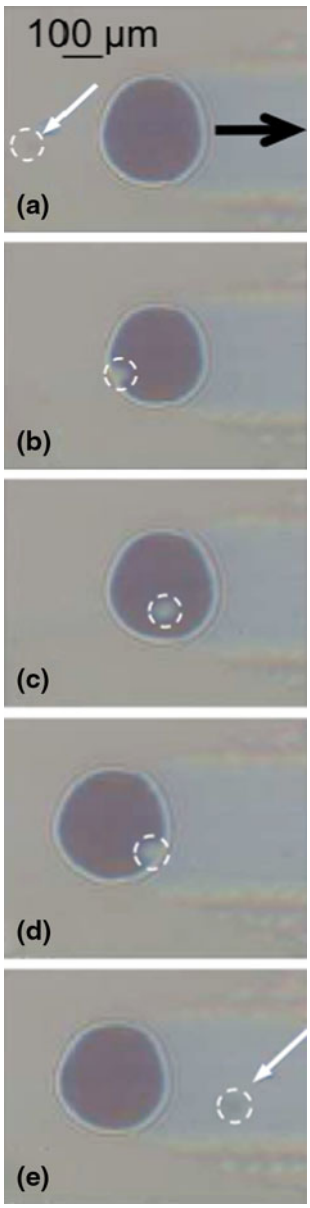

Fig. 9 In situ propagation of the carbon nanotubes in the contact in pure rolling conditions. The *white arrow* in **a** indicates the aggregate to follow in the inlet zone. The aggregate penetrates in the conjunction (**b**), travels through (**c**), leaves (**d**) and passes through the outlet zone (**e**). The *black arrow* in (**a**) indicates the flow direction from the left to the right

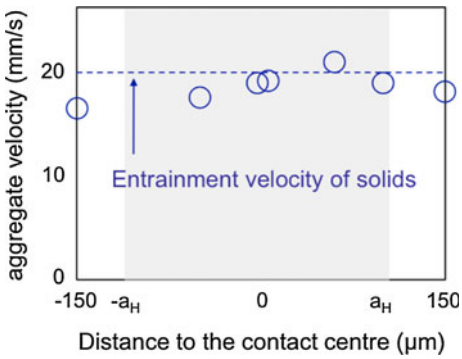

Fig. 10 In situ entrainment velocity of the aggregates compared to that of the solids (in *dashed lines*) from the inlet to the outlet zone. The size of the contact zone from $-a_H$ to a_H is indicated by means of the *grey* area

fluid under pressure or a slip at the wall phenomenon [6, 46]. In this framework, we seem to show that the transient local increase in thickness, which is a signature of the aggregate passage, tends to travel slower than the entrainment. If the diminution of the propagation velocity of the carbon nanotubes compared to that of the solids is not due to the lack of measurement precision, it might be attributed to a viscous damping effect of the fluid under pressure.

3.4 Frictional Behaviour of the Dispersions

Figure 11 demonstrates the impact of carbon nanotubes on the friction behaviour of the lubricants. An entrainment velocity $U_e = 0.02$ m/s was chosen to ensure that aggregates travel through the contact and there is an increase in the central film thickness and also to avoid the occurrence of starvation for highly concentrated dispersions. It is clear from Fig. 11 that the introduction of carbon nanotubes

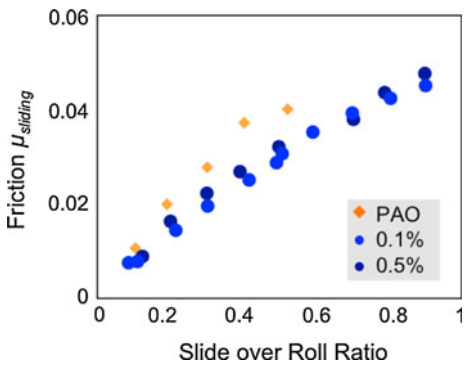

Fig. 11 Evolution of the sliding friction coefficient $\mu_{sliding}$ as a function of the SRR at a constant entrainment velocity, $U_e = 20$ mm/s, and contact pressure $P \sim 305$ MPa. We can detect a strong impact of the presence of carbon nanotubes independently of the concentration. A shift in the onset of wear towards higher SRR occurrence is also observed for the carbon-nanotube dispersions

induces a reduction of friction as a function of the SRR, compared to that obtained with the PAO base oil, at slow sliding velocity. Moreover, this friction reduction is independent of the carbon-nanotube concentration.

Note that first wear scars were observed on the disc surface for SRRs over 60 % for the PAO base oil although the onset of wear was delayed to a SRR of over 80 % in the presence of carbon nanotubes (not shown here, see [29]).

4 Discussion

4.1 Film-Forming Mechanisms: What Happens in the Inlet Zone?

The conditions in the inlet zone where the pressure is low and hydrodynamic conditions prevail mainly control the film-forming mechanisms. The work of Colacicco [3, 4] and Meunier [6, 7] focused on soot aggregation in lubrication. They both showed that an overconcentration of soots in the convergent zone can result in a higher viscosity and thus lead to a thicker central film thickness. However, the considered soot concentrations are rather high compared to the carbon-nanotube concentrations at stake here, leading to a larger increase in the bulk viscosity than that observed in our case. We can also assume that the piezoviscous coefficient remains constant with addition of carbon nanotubes for the concentrations considered. According to Hamrock–Dowson's theory for piezoviscous fluids [45], the knowledge of the viscosity in the inlet zone and the piezoviscosity of a lubricant allows for the determination of its fully flooded film thickness for given experimental conditions. Reciprocally, knowing the film thickness at entrainment velocities low enough to ensure fully flooded conditions, leads to the apparent viscosity in the convergent zone as seen by the contact. This approach gives an apparent viscosity close to that of the base oil for the 0.5 % (w/w) dispersion, lower than that measured by rheometry: this could mean that the concentration of carbon nanotubes in the inlet zone differs from that of the bulk. Figure 12a–c presents the trajectory of large aggregates (indicated with the blue arrow) at the contact periphery: in a zone larger than 120 µm over the contact area, they seem to travel away from the conjunction and their velocity is of the same order of magnitude as that of aggregates travelling through (indicated with the white arrow). This also seems consistent with the critical size of aggregates in the contact.

In pure rolling conditions, these observations can be tentatively explained using an analysis of flow and back flow streamlines in an EHL contact as described in [1, 47, 48]. The flow is divided into two regions in the contact inlet: the first region near the surfaces is where the flow

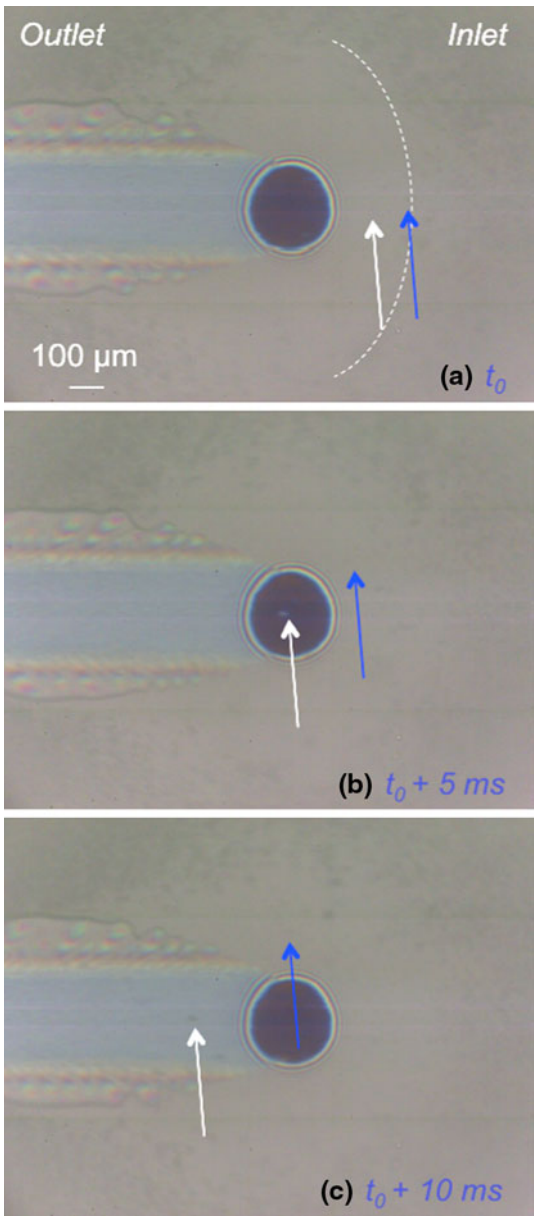

Fig. 12 Trajectory of large aggregates at the contact periphery. The *white arrow* follows a small aggregate, while the *blue arrow* shows a large one. It can be seen from (**a**) to (**c**) that small aggregates pass through the conjunction and large ones deviate to the sides of the contact. A zone of about 120 µm around the contact area can be depicted. The time interval between each interferogram is 5 ms and the flow goes from left to right

passes through the contact and the second region is the reverse- or back-flow where the flow is partly rejected from the contact due to the formation of two vortices. The frontier between these two regions is where the fluid forces acting on a particle are balanced [1]: a particle located in the first region has a high probability of being entrained into the contact while it will be rejected in the second region. The location of the frontier or stagnation point depends on the entrainment velocity: an increase in velocity will induce an enlargement of the back-flow region to the detriment of the zone of flow. The number of particles likely to be entrained in the conjunction diminishes. This analysis tends to explain what we observe in this study: at entrainment velocities slower than 0.04 m/s, aggregates of carbon nanotubes are detected in the conjunction although they remain undetected at faster entrainment—due to inadequate time resolution. Besides, an associated increase in film thickness also contributes to make the aggregate observation difficult: at fast entrainment, the central film thickness is higher than 100 nm.

Microscopic observations show that aggregates thicker than 100 nm exist in the dispersions. However, they remain undetected in the conjunction. This might be explained by a destructuring effect of large aggregates induced by high shear rates in the convergent zone. Nevertheless, large aggregates are depicted near the conjunction zone and their trajectory is presented in Fig. 12. This tends to demonstrate that only aggregates thinner than 100 nm reach the inlet zone and specifically the flow region although those thicker than 100 nm are rejected from the contact in the back-flow region. The contact inlet, that governs the film thickness, seems to act as filter of aggregates.

4.2 Influence of Shear on Film Formation

At constant entrainment velocity, interferograms in Fig. 13 illustrate the influence of the increasing sliding velocity on both the central film thickness and the number of carbon nanotubes entrained in the contact for the 0.5 % (w/w) dispersion. Figure 14a quantitatively plots the dependence of the film thickness with the sliding velocity for the PAO base oil and the 0.5 % (w/w) concentrated dispersion: the central film thickness decreases with an increasing sliding

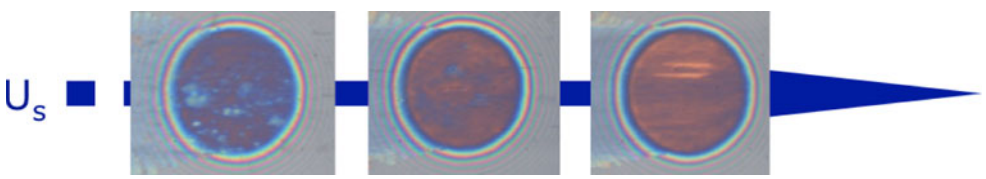

Fig. 13 Contact interferograms showing the influence of shear U_s on the film thickness and the number of aggregates penetrating in the contact at constant entrainment velocity, $U_e = 20$ mm/s. Both the film thickness and the number of aggregates decrease as shear increases

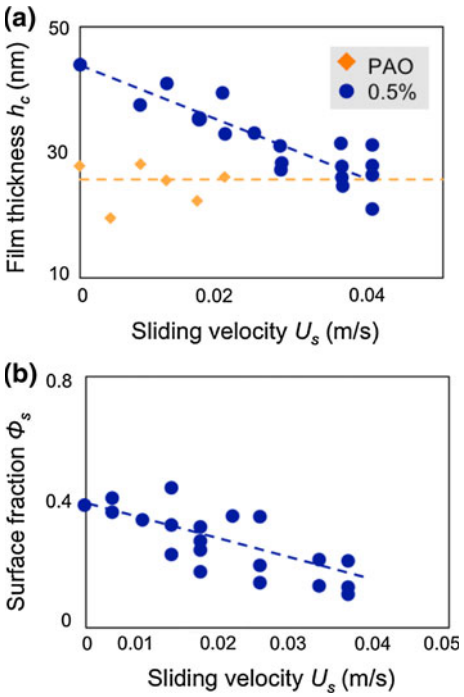

Fig. 14 Quantitative dependence of **a** film thickness and **b** surface fraction of aggregates with the sliding velocity U_s for the 0.5 % (w/w) dispersion and the PAO

velocity in the case of the dispersion while it remains constant for the PAO base oil. This tendency can be quantitatively described using

$$h_c = h_{PAO} + t_0(U_c - U_s), \tag{2}$$

where U_c and t_0 are constant. t_0 is a characteristic time equal to 4×10^{-7} s and U_c is the velocity beyond which the dispersion film thickness is equal to that of the PAO, i.e., 0.05 m/s. h_{PAO} represents the value of the PAO film thickness.

The number of aggregates penetrating the conjunction also varies with the sliding velocity as presented in Fig. 14b in terms of the surface fraction occupied by aggregates over the whole contact. The surface fraction is calculated from the ratio between the surface occupied by aggregates and that of the contact. It clearly shows that the surface fraction strongly diminishes from 40 % to reach 0 at a U_s of 0.05 m/s. Similarly, one can consider that

$$\phi_s = \phi_0 - \frac{U_s}{U_0}, \tag{3}$$

where ϕ_0 is the surface fraction corresponding to $U_s = 0$ and U_0 is a characteristic velocity equals to 0.14 m/s. The introduction of sliding induces a modification of the forces experienced by the particles in the inlet zone: the stagnation point shifts towards the slower moving surface and make the flow asymmetrical as presented in [1]. In our experiments, we distinguish no or little difference in the surface fraction occupied by the aggregates penetrating the conjunction as a function of the nature of the slower moving surfaces. This may be due to the low interactions between the surfaces and the carbon nanotubes. No significant difference between C^+ and C^- was observed. Another difference emerges from the introduction of sliding: in Poiseuille flow, the particles migrate and move near the surfaces due to the forces of the fluid while in a Couette flow, these particles remain in the flow central line [1]. With introduction of sliding, the Couette flow is increased: some of the particles may be pushed to reverse-flow streamlines. This could explain the enhanced rejection of particles from the contact inlet as observed in Figs. 13 and 14b.

4.3 Friction-Reduction Mechanisms

4.3.1 How Can We Account for the Reduction of Friction Observed with the Carbon Nanotubes?

The first assumption to consider is that nanotubes aggregates locally lift the two surfaces while located in the contact and thus improve the load-bearing capacity compared to that of PAO. Pure rolling experiments at low entrainment velocity show that the stabilized central film thickness increases from 10 to 40 nm with the aggregate concentration, respectively, for the 0.01 and 0.5 % (w/w) dispersions. This effect is not correlated to the lubricant viscosity in this considered range of velocities but to the surface fraction of aggregates within the contact. Rolling–sliding experiments also evidence the correlation, as presented in Fig. 15, where the ratio between the 0.5 % (w/w) dispersion central film thickness and that of the PAO is plotted as a function of the surface fraction ϕ_s at $U_e = 0.02$ m/s. Its evolution can therefore be calculated as a function of the characteristic constants U_c, U_0, t_0 and the surface fraction ϕ_s combining Eqs. (2) and (3)

$$U_s = U_0(\phi_0 - \phi_s) \tag{4}$$

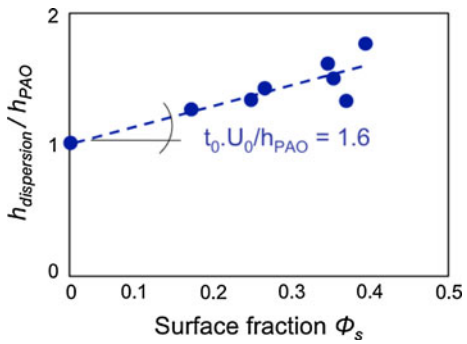

Fig. 15 Evolution of the ratio between the central film thickness of the 0.5 % (w/w) dispersion and that of the PAO vs the surface fraction. A linear relation can be established (see Eq. 6)

$$h_c = h_{PAO} + t_0(U_c - U_0 \cdot \phi_0) + t_0 \cdot U_0 \cdot \phi_s, \quad (5)$$

which gives

$$\frac{h_c}{h_{PAO}} = 1 + \frac{t_0}{h_{PAO}}(U_c - U_0 \cdot \phi_0) + \frac{t_0 \cdot U_0}{h_{PAO}}.\phi_s \approx 1 + \frac{t_0 \cdot U_0}{h_{PAO}}.\phi_s. \quad (6)$$

Numerical application confirms that $\frac{t_0}{h_{PAO}}(U_c - U_0 \cdot \phi_0) \ll 1$ and that $\frac{t_0 \cdot U_0}{h_{PAO}} \approx 2$ as obtained in Fig. 15. In this framework, the increase in central film thickness leads to a decrease of the shear rate and thus to a reduction in friction at low sliding velocity (high surface fraction).

We can thus propose an additive friction law considering a multi-phasic contact composed of base oil and carbon-nanotube aggregates as schematically depicted in Fig. 16a. The total shear stress results from a contribution due to the shear of carbon-nanotube aggregates within the contact and another contribution from the sheared base oil. The total shear stress, $\tau_{dispersion}$, can be calculated from

$$\tau_{dispersion} = \phi_s.\tau_{CNT} + (1 - \phi_s).\tau_{PAO}, \quad (7)$$

where τ_{CNT} is the shear stress of the carbon-nanotube aggregates, τ_{PAO} is the shear stress of the PAO and ϕ_s is the surface fraction of carbon-nanotube aggregates in the contact. In addition, in EHL, the friction induced by sliding depends on the rheological behaviour of the lubricant film under pressure confined between the solid surfaces. This means that $\tau_{dispersion}$, τ_{CNT} and τ_{PAO} are expected to vary with the sliding velocity and the contact pressure. Figure 16b presents the evolution of the mean shear stress of the PAO and for the 0.5 % (w/w) dispersion as a function of the sliding velocity: both curves first increase linearly with the sliding velocity before they bend off to reach the plastic limiting shear stress at approximately 25 MPa, represented with a dashed line in Fig. 16b, for the PAO base oil. This high value could be related to solid/solid contacts since wear onset was depicted from a 60 % SRR. The slope of the curves at low sliding velocity is, respectively, equals to 8×10^8 and 6.10^8 Pa s m^{-1} for the PAO and the dispersion. We can assume that friction mainly originates from viscous contribution for the PAO, that is to say

$$\tau_{PAO} = \frac{\eta_{PAO,P} \cdot U_s}{h_c}, \quad (8)$$

where $\eta_{PAO,P}$ is the viscosity under pressure of the PAO that can be estimated using the Barus' law and h_c is the central film thickness. Numerical application gives

$$\tau_{PAO} = \frac{\eta_{PAO,P} \cdot U_s}{h_c} \approx 9 \times 10^8 \cdot U_s \quad (9)$$

in good agreement with the slope on the PAO curve in Fig. 16b. In the case of the carbon-nanotube aggregates, the local increase in load-bearing suggests that they are more likely to contribute elastically to shear. The shear stress τ_{CNT} can then be calculated from

$$\tau_{CNT} = \frac{2a_H}{U_e} \cdot G \cdot \frac{U_s}{h_{CNT}}, \quad (10)$$

where G is the shear elastic modulus and h_{CNT} is the thickness of an aggregate in the contact that is constant at 100 nm. Combining Eqs. (2), (3), (8) and (10), Eq. (7) becomes

$$\tau_{dispersion} = \frac{[(U_0 - U_0 \cdot \phi_0)\,\eta_{PAO,P} \cdot U_s + \eta_{PAO,P} \cdot U_s^2]}{U_0[h_{PAO} + t_0(U_c - U_s)]} + \frac{2a_H}{U_e} \cdot G \cdot \frac{U_s}{h_{CNT}} \cdot \phi_0 - \frac{2a_H}{U_e} \cdot \frac{G}{U_0} \cdot \frac{U_s^2}{h_{CNT}}. \quad (11)$$

From the experimental slope $(d\tau_{dispersion}/dU_s)_{U_s=0}$ of the 0.5 % (w/w) curve in Fig. 16b and the knowledge of ϕ_0,

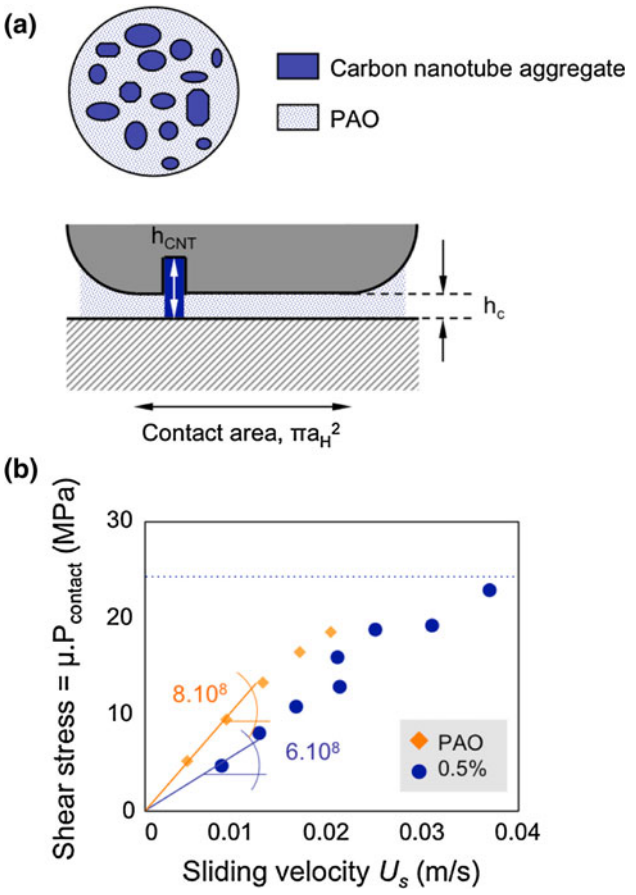

Fig. 16 **a** Schematic representation of the sheared interface lubricated with a carbon-nanotube dispersions (*top view* and profile). **b** Shear stress versus shear rate for the PAO base oil (*filled triangle*) and the high concentrated dispersion (0.5 % (w/w) in *filled circle*). The apparent viscosity under pressure ($P \sim 305$ MPa) of the base oil can be determined from the linear slope indicated with a *continuous line*. The *dashed line* represents the plastic limiting shear stress for the PAO

$\eta_{PAO,P}$, h_{PAO}, t_0, U_c, a_H, U_e and h_{CNT}, one can estimate the shear elastic modulus G as

$$\left(\frac{d\tau_{dispersion}}{dU_s}\right)_{U_s=0} = \frac{(1-\phi_0)\cdot\eta_{PAO,P}}{h_{PAO}+t_0\cdot U_c} + \frac{2a_H}{U_e}\cdot\frac{\phi_0}{h_{CNT}}\cdot G. \quad (12)$$

Numerical application gives $G = 6 \times 10^3$ Pa. This is a right order of magnitude taking into account the high concentration of the aggregate and the contact pressure at about 305 MPa [29].

However, if one assumes that the aggregates contribution to shear is viscous, the shear stress τ_{CNT} becomes

$$\tau_{CNT} = \eta_{CNT,P}\cdot\frac{U_s}{h_{CNT}}, \quad (13)$$

where $\eta_{CNT,P}$ is the viscosity under pressure of the carbon-nanotube aggregate. Following the same methodology, we obtain

$$\tau_{dispersion} = \frac{\left[(U_0 - U_0\cdot\phi_0)\,\eta_{PAO,P}\cdot U_s + \eta_{PAO,P}\cdot U_s^2\right]}{U_0[h_{PAO}+t_0(U_c-U_s)]} + \eta_{CNT,P}\cdot\frac{U_s}{h_{CNT}}\cdot\phi_0 - \frac{\eta_{CNT,P}}{U_0}\cdot\frac{U_s^2}{h_{CNT}} \quad (14)$$

$$\left(\frac{d\tau_{dispersion}}{dU_s}\right)_{U_s=0} = \frac{(1-\phi_0)\,\eta_{PAO,P}}{h_{PAO}+t_0\cdot U_c} + \frac{\phi_0}{h_{CNT}}\cdot\eta_{CNT,P}. \quad (15)$$

Numerical application gives $\eta_{CNT,P} = 75$ Pa s which corresponds to an aggregate viscosity under ambient pressure of roughly 150 mPa s according to Barus' law. De Gennes proposed a scale law to describe polymer solutions in semi-dilute regime [49]. In this framework, using an analogy between carbon nanotubes and polymer, the viscosity follows the concentration with a power law of exponent 5/4. This would lead us to estimate the local concentration of the aggregates at 1 % (w/w). This value is also coherent [29].

It is more likely that aggregates contribute both elastically and viscously to shear. Then the total shear stress $\tau_{dispersion}$ takes the more complex form

$$\tau_{dispersion} = \frac{\left[(U_0 - U_0\cdot\phi_0)\,\eta_{PAO,P}\cdot U_s + \eta_{PAO,P}\cdot U_s^2\right]}{U_0[h_{PAO}+t_0(U_c-U_s)]} + \eta_{CNT,P}\cdot\frac{U_s}{h_{CNT}}\cdot\phi_0 - \frac{\eta_{CNT,P}}{U_0}\cdot\frac{U_s^2}{h_{CNT}} + \frac{2a_H}{U_e}\cdot\frac{U_s}{h_{CNT}}\cdot G\cdot\phi_0 - \frac{2a_H}{U_e}\cdot\frac{G}{U_0}\cdot\frac{U_s^2}{h_{CNT}} \quad (16)$$

and

$$\left(\frac{d\tau_{dispersion}}{dU_s}\right)_{U_s=0} = \frac{(1-\phi_0)\,\eta_{PAO,P}}{h_{PAO}+t_0\cdot U_c} + \frac{\phi_0}{h_{CNT}}\left(\eta_{CNT,P} + \frac{2a_H}{U_e}\cdot G\right). \quad (17)$$

Unfortunately, we are unable to numerically decouple the elastic and viscous contributions. Nevertheless, previous calculations give an overestimate of both contributions.

However, the fact that aggregates improve the load-bearing capacity is a striking result that is not commonly observed. In addition, all the scenarios strongly highlight the role of the nanotubes and their rheology at low sliding velocity on friction behaviour. As sliding increases, fewer aggregates penetrate in the contact. At high sliding velocity, the behaviour of the dispersion is governed by the rheology of the base oil. For intermediate U_s, the evolution of the total shear stress results from a balance of both previous contributions. The balance is related to the surface fraction and diminishes as the velocity increases.

5 Conclusions

This experimental approach has allowed the simultaneous measurement of the film thickness and its heterogeneity and the frictional properties of carbon-nanotube dispersions in elastohydrodynamic lubrication regime. We believe that it brings a better insight into the lubrication mechanisms in colloidal fluids.

First, under pure rolling conditions, the film-forming ability is function of the concentration of carbon nanotubes. At low concentration, the film thickness is governed by the viscosity of the lubricant, as predicted by EHL theory. At high concentration, starvation occurs at high velocity due to the heterogeneity of the dispersion. It results in a reduction of film thickness. However, the carbon-nanotube aggregates penetrate and travel through the EHL conjunction. The carbon nanotubes are chemically inert and do not adsorb on the considered surfaces. The in situ visualization at low velocity shows an induced local transient increase in thickness at approximately 100 nm, independently of the concentration. Therefore, one can assume that the contact inlet behaves as a filter of aggregates. In addition, the in situ visualization associated with high-speed recording camera allows one to quantitatively describe the carbon-nanotube aggregate propagation in terms of velocity distribution along the contact: they slow down in the first half of the conjunction in relation with possible damping viscous effect.

In a second step, the frictional behaviour of the dispersions has been determined by means of sliding experiments and is accounted for using the interface rheology under pressure and an additive friction law depicting the instantaneous multi-phasic contact as composed of base oil and carbon-nanotube aggregates. We conclude that the addition of carbon nanotubes clearly reduces the friction. This originates from the transient passage of the aggregates in

the contact. At low sliding velocity, the aggregates propagate easily within the contact and their presence control the friction response. At high sliding velocity, shear induces a reduction of the number of aggregates passing through the contact and the friction response is dominated by the rheological behaviour of the base oil under pressure.

Acknowledgments The authors acknowledge Prof. Hugh Spikes from Imperial College London for fruitful discussions. We thank Dr. Julien Amadou from Nanocyl and Dr. Raphaèle Iovine from Total France for technical and financial supports. Thanks are also due to the CLYM—http://clym.insa-lyon.fr—for the access to the 2010F microscope and Béatrice Vacher for technical support.

References

1. Chinas-Castillo, F., Spikes, H.A.: Mechanism of action of colloidal solid dispersions. J. Tribol. **125**, 552–557 (2003)
2. Chinas-Castillo, F., Spikes, H.A.: The behavior of diluted sooted oils in lubricated contacts. Tribol. Lett. **16**, 317–322 (2004)
3. Colacicco, Ph.: Role de l'agrégation des suies sur la lubrification des moteurs diesel. PhD thesis, École Centrale de Lyon (1992)
4. Colacicco, Ph, Mazuyer, D.: The role of soot aggregation on the lubrication of diesel engines. Tribol Trans. **38**, 959–965 (1995)
5. Varenne, E.: Usure de la distribution d'un moteur diesel. PhD thesis, École Centrale de Lyon (1996)
6. Meunier, C.: Vieillissement des lubrifiants et compréhension des mécanismes de dégradation: application à la zone segment-piston-chemise. PhD thesis, École Centrale de Lyon (2008)
7. Meunier, C., Mazuyer, D., Vergne, Ph, El Fassi, M., Obiols, J.: Correlation between the film forming ability and rheological properties of new and aged low sulfated ash, phosphorus and sulfur (Low SAPS) automotive lubricants. Tribol Trans. **52**, 501–510 (2009)
8. Ostwald, W.: An Introduction to theoretical and applied colloid chemistry, 2nd edn. Wiley, New York (1922)
9. Israelachvili, J.: Intermolecular and surface forces, 2nd edn. Academic Press, London (1991)
10. Cusano, C., Sliney, H.E.: Dynamics of solid dispersions in oil during the lubrication of point contacts. ASLE Trans. **25**, 183–189 (1981)
11. Palios, S., Cann, P.M, Spikes, H.A.: Behaviour of PTFE suspensions in rolling/sliding contacts. In: Dowson, D., et al. Proceedings of Leeds Lyon 22. Tribology Series, vol. 31, pp. 141–152. Elsevier (1996)
12. Wan, G.T.Y., Spikes, H.A.: The behavior of suspended solid particles in rolling and sliding EHL contacts. STLE Trans. **31**, 12–21 (1988)
13. Genin, C.: Optimisation de systèmes colloidaux en phase aqueuse pour la lubrification en conditions extremes: application au tréfilage. PhD thesis, École Centrale de Lyon (2007)
14. Genin, C., Mazuyer, D., Monin, D.: Study of the influence of the interactions between wax particles and surfaces on the properties of thin lubricating films in a high-pressure contact. Tribol Trans. **50**, 374–386 (2007)
15. Hollinger, S., Georges, J.M., Mazuyer, D., Lorentz, G., Aguerre, O., Nguyen, Du: High pressure lubrication with lamellar structures in aqueous lubricant. Tribol. Lett. **9**(3–4), 143–151 (2000)
16. Rapoport, L., Leshchinsky, V., Lapsker, I., Volovik, Y., Nepomnyashchy, O., Lvovsky, M., Popovitz-Biro, R., Feldman, Y., Tenne, R.: Tribological properties of WS_2 nanoparticles under mixed lubrication. Wear **255**, 785–793 (2003)
17. Radice, S., Milscher, S.: Effect of electrochemical and mechanical parameters on the lubrication behaviour of Al_2O_3 nanoparticles in aqueous suspensions. Wear **261**, 1032–1041 (2006)
18. Hu, Z.S., Lai, R., Lou, F., Wang, L.G., Chen, Z.L., Dong, J.X.: Preparation and tribological properties of nanometer magnesium borate as lubricating oil additive. Wear **252**, 370–374 (2002)
19. Zhou, X.: Study on the tribological properties of surfactant-modified MoS_2 micrometer spheres as an additive in liquid paraffin. Tribol Int. **40**, 863–868 (2007)
20. Dong, J.X., Hu, Z.S.: A study of the anti-wear and friction-reducing properties of the lubricant additive nanometer zinc borate. Tribol Int. **31**, 219–223 (1998)
21. Hu, Z.S., Dong, J.X.: Study on antiwear and reducing friction additive of nanometer titanium oxide. Wear **216**, 92–96 (1998)
22. Hu, Z.S., Dong, J.X., Chen, Z.L.: Study on antiwear and reducing friction additive of nanometer ferric oxide. Tribol Int. **31**, 355–360 (1998)
23. Cizaire, L.: Lubrification limite par les nanoparticules. PhD thesis, École Centrale de Lyon (2003)
24. Joly-Pottuz, L.: Nanoparticules lubrifiantes à structure fermée. PhD thesis, École Centrale de Lyon (2006)
25. Rapoport, L., Leshchinsky, V., Lapsker, I., Verdyan, A., Moshkovich, A., Feldman, Y., Tenne, R.: Behavior of fullerene-like WS_2 nanoparticles under severe contact conditions. Wear **259**, 703–707 (2005)
26. Rosentsveig, R., Gorodnev, A., Feuerstein, N., Friedman, H., Zak, A., Fleischer, N., Tannous, J., Dassenoy, F., Tenne, R.: Fullerene-like MoS_2 nanoparticles and their tribological behavior. Tribol. Lett. **36**, 175–182 (2009)
27. Tannous, J., Dassenoy, F., Lahouij, I., Le-Mogne, T., Vacher, B., Bruhacs, A., Tremel, W.: Understanding the tribological mechanisms of IF-MoS_2 nanoparticles under boundary lubrication. Tribol. Lett. **41**, 55–64 (2011)
28. Kroto, H.W., Heath, J.R., O'Brien, S.C., Curl, R.F., Smalley, R.E.: C60: Buckminsterfullerene. Nature **318**, 162–163 (1985)
29. Chauveau, V.: Le pouvoir lubrifiant des nanotubes de carbone. PhD thesis, École Centrale de Lyon (2010)
30. Bushan, B., Gupta, B.K., Van Cleef, G.W., Capp, C., Coe, J.V.: Fullerenes C60 films for solid lubrication. Tribol Trans. **36**, 573–580 (1993)
31. Bushan, B., Gupta, B.K., Van Cleef, G.W., Capp, C., Coe, J.V.: Sublimed C60 films for tribology. Appl. Phys. Lett. **62**, 3253–3255 (1993)
32. Tannous, J., Dassenoy, F., Bruhacs, A., Tremel, W.: Synthesis and tribological performance of novel Mo_xW_{1-x} S_2 ($0 \leq x \leq 1$) inorganic fullerenes. Tribol. Lett. **37**, 83–92 (2010)
33. Falvo, M.R., Taylor II, R.M., Helser, A., Chi, V., Brooks Jr, F.P., Washburn, S., Superfine, R.: Nanometre-scale rolling and sliding of carbon nanotubes. Nature **397**, 236–238 (1999)
34. Ohmae, N., Martin, J.M., Mori, S.: Micro and nanotribology. ASME Press, New York (2005)
35. Mylvaganam, K., Zhang, L.C., Xiao, K.Q.: Origin of friction in films of horizontally oriented carbon nanotubes sliding against diamond. Carbon **47**, 1693–1700 (2000)
36. Ni, B., Sinnott, S.: Tribological properties of carbon nanotube bundles predicted from atomistic simulations. Surf. Sci. **487**, 87–96 (2001)
37. Buldum, A., Lu, J.P.: Atomic scale sliding and rolling of carbon nanotubes. Phys. Rev. Lett. **83**, 5050–5053 (1999)
38. Chen, C.S., Chen, X.H., Hu, J., Zhang, H., Xu, L.S., Yang, Z.: Effect of multi-walled carbon nanotubes on tribological properties of lubricant. Trans. Nonferrous Met. Soc. China **15**, 300–305 (2005)
39. Chen, C.S., Chen, X.H., Xu, L.S., Yang, Z., Li, W.H.: Modification of multi-walled carbon nanotubes with fatty acid and their

tribological properties as lubricant additive. Carbon **43**, 1660–1665 (2005)
40. Saint-Aubin, K., Poulin, Ph, Saadaoui, H., Maugey, M., Zakri, C.: Dispersion and film-forming properties of poly(acrylic acid)-stabilized carbon nanotubes. Langmuir **25**, 13206–13211 (2009)
41. Bou-Chakra, E., Cayer-Barrioz, J., Mazuyer, D., Jarnias, F., Bouffet, A.: A non-Newtonian model based on Ree–Eyring theory and surface effect to predict friction in elastohydrodynamic lubrication. Tribol Int. **43**, 1674–1682 (2010)
42. Fay, H., Cayer-Barrioz, J., Mazuyer, D., Mondain-Monval, O., Ponsinet, V., Meeker, S.: Lubrication mechanisms of lamellar fatty acid fluids. Tribol. Lett. **46**, 285–297 (2012)
43. Bouré, Ph.: Lubrification et usure du contact fil/outil en tréfilage humide. PhD thesis, École Centrale de Lyon (1999)
44. De Vicente, J., Stokes, J.R., Spikes, H.A.: The frictional properties of Newtonian fluids in rolling–sliding soft-EHL contact. Tribol. Lett. **20**, 273–286 (2005)
45. Hamrock, B.J., Dowson, D.: Isothermal elastohydrodynamic lubrication of point contacts. NASA Technical notes D8318, 1–31 (1976)
46. Reddyhoff, T., Spikes, H.A., Choo, J.H., Glovnea, R.P.: Lubricant flow in an elastohydrodynamic contact using fluorescence. Tribol. Lett. **38**, 207–215 (2010)
47. Hamrock, B.J., Schmid, S.R., Jacobson, B.O.: Fundamentals of fluid film lubrication, 2nd edn. Marcel Dekker, Inc, New York (2004)
48. Tipei, N.: Boundary conditions of a viscous flow between surfaces with rolling and sliding motion. J. Lubr. Technol. F **90**, 254–261 (1968)
49. De Gennes, P.G.: Scaling concepts in polymer physics. Cornell University Press, New York (1979)